PHYSICAL REVIEW E **101**, 023207 (2020)

Sculpted ultracold neutral plasmas

Vikram S. Dharodi[*] and Michael S. Murillo[†]
Department of Computational Mathematics, Science, and Engineering, Michigan State University, East Lansing, Michigan 48824, USA

(Received 8 April 2019; revised manuscript received 6 January 2020; accepted 3 February 2020; published 19 February 2020)

Ultracold neutral plasma (UNP) experiments allow for careful control of plasma properties across Coulomb coupling regimes. Here, we examine how UNPs can be used to study heterogeneous, nonequilibrium phenomena, including nonlinear waves, transport, hydrodynamics, kinetics, stopping power, and instabilities. Through a series of molecular dynamics simulations, we have explored UNPs formed with spatially modulated ionizing radiation. We have developed a computational model for such sculpted UNPs that includes an ionic screened Coulomb interaction with a spatiotemporal screening length, and Langevin-based spatial ion-electron and ion-neutral collisions. We have also developed a hydrodynamics model and have extracted its field quantities (density, flow velocity, and temperature) from the molecular dynamics simulation data, allowing us to investigate kinetics by examining moment ratios and phase-space dynamics; we find that it is possible to create UNPs that vary from nearly perfect fluids (Euler limit) to highly kinetic plasmas. We have examined plasmas in three geometries: a solid rod, a hollow rod, and a gapped slab; we have studied basic properties of these plasmas, including the spatial Coulomb coupling parameter. By varying the initial conditions, we find that we can design experimental plasmas that would allow the exploration of a wide range of phenomena, including shock and blast waves, stopping power, two-stream instabilities, and much more. Using an evaporative cooling geometry, our results suggest that much larger Coulomb couplings can be achieved, possibly in excess of 10.

DOI: 10.1103/PhysRevE.101.023207

I. INTRODUCTION

Knowledge of the physics of nonideal plasmas [1] is important both at a fundamental level, to understand how correlations and collisions impact plasma properties, and for a wide range of applications, including astrophysics [1–3], pulsed power [4–6], inertially confined plasmas [7], and laser-excited solids [8–12], among other applications. Over the past few decades, remarkable progress has been made in the areas of convergent collision theories [13], equations of state [14–16], and transport properties [17–19]. However, the plasma properties that have been studied are primarily relevant for macroscopically homogeneous and isotropic plasmas, whereas real plasmas tend to have important density gradients and transient behavior, as in the cases of implosion dynamics in inertial-confinement fusion experiments [20] and of shocks and instabilities [21,22], in general. It is therefore of interest to examine the macroscopic, nonequilibrium properties of nonideal plasmas across Coulomb coupling regimes.

Ideally, what is desired is an experimental platform that offers precise control over the density, temperature, ionization state, and initial density profile of a plasma. Ultracold neutral plasmas (UNPs) [23] offer a promising platform that meets these requirements. UNPs are formed by photoionizing a cold (typically millikelvin), neutral, trapped gas [24–27], allowing the Coulomb coupling to be varied over the weakly to moderately coupled regime. Through the choice of density, the gas-cooling process, and the intensity of the photoionization laser, the ionic density and temperature can be controlled; the wavelength of the laser can be used to independently control the electron temperature. Because of this level of control of the ionization process, UNPs have a well-defined ionization of unity, and doubly ionized UNPs can also be created [28]. Moreover, UNP mixtures can be created [29]. Importantly for this paper, it is possible to modulate the ionization laser spatially by using a mask to create a UNP with a desired initial density distribution [30,31]; we will refer to such UNPs as sculpted ultracold neutral plasmas (SUNPs). Thus, UNPs offer a unique platform for creating well-controlled and well-diagnosed plasmas.

Our goal is to examine how the use of masks in the photoionization process can be exploited to explore a wide range of physical phenomena. Specifically, we wish to examine how sculpting the initial state can create well-diagnosed plasmas that are sensitive to isolated properties of interest. We achieve this through nonequilibrium molecular dynamics (NEMD) simulations. We have developed an NEMD model that evolves heterogeneous ions from an initial spatial configuration in the presence of background electrons and neutrals, which are implicitly included through a spatial Langevin model. While it is established that the Yukawa model is fairly accurate for homogeneous UNPs, we introduce two modifications that allow the use of a spatiotemporally varying screening length [32] in

---

[*] dharodiv@msu.edu
[†] murillom@msu.edu

molecular dynamics (MD), and we use an electronic energy equation that accounts for electronic temperature changes arising from those variations. With this model of UNPs, we explore the physics of hydrodynamics, including the perfect-fluid limit, as well as kinetic processes associated with beams, such as stopping power and two-stream instabilities; we explore these processes in the contexts of three different initial density distributions.

This paper is organized as follows. In Sec. II, we introduce our computational model for heterogeneous UNPs. Next, in Sec. III, we discuss a coarse-graining procedure that allows us to obtain hydrodynamic information from our MD simulations, and we discuss metrics for quantifying closeness to equilibrium. A simple hydrodynamic model is then introduced in Sec. IV and is employed to examine whether choices for the initial sculpted density correspond to the perfect-fluid limit or to a highly kinetic plasma. In Sec. V, we discuss how the simulations are initialized and show the results of the simulations. Finally, in Sec. VI, we discuss our results and offer concluding remarks.

II. PLASMA MODEL

The Yukawa model has been used very successfully to model many properties of ultracold plasmas [33,34] with MD. However, for heterogeneous, nonequilibrium plasmas, several of the assumptions of the Yukawa model fail. In particular, the screening length is not constant in either time or space, and the electrons play an energetic role as a result [35–37]. In addition, the ions exchange energy with the hotter electrons, which surround the ions, and with the cooler residual neutrals, which the ions encounter as they move into nonionized regions. Here, we develop a model that improves upon these defects of the Yukawa model while still avoiding an explicit evolution of the electrons (either through MD or through a hybrid fluid-MD approach) [38], which we leave to future work. The cgs system of units is used in everything that follows. Also, quantities that are typically constant but taken as time dependent in this paper will have a time argument; in the next section, these quantities will be further generalized to field quantities that depend on space and time.

We formulate the model in terms of a Hamiltonian $\mathcal{H}$ for all of the species in the UNP, which is modeled as a three-species plasma composed of ions (i), electrons (e), and neutrals (n). The Hamiltonian $\mathcal{H}$, neglecting neutral-neutral and electron-neutral interactions, is the sum of the kinetic energies K_α, intraspecies potential energies $U_{\alpha\alpha}$, and interspecies potential energies $U_{\alpha\beta}$ over α and β species:

$$\mathcal{H} = K_i + K_e + U_{ee} + U_{ii} + U_{ie} + U_{in}. \tag{1}$$

We wish to avoid the computational expense of directly simulating the electrons and neutrals, so we begin with the equations of motion for the ions, which are

$$\dot{\mathbf{r}}_j = \frac{\mathbf{p}_j}{m_j}, \tag{2}$$

$$\dot{\mathbf{p}}_j = -\frac{\partial U_{ii}}{\partial \mathbf{r}_j} - \frac{\partial U_{ie}}{\partial \mathbf{r}_j} - \frac{\partial U_{in}}{\partial \mathbf{r}_j} = \mathbf{F}_{ii} + \mathbf{F}_{ie} + \mathbf{F}_{in}. \tag{3}$$

In the right-hand side (RHS) of Eq. (3), the first term $\mathbf{F}_{ii}$ describes the ion-ion interactions; the corresponding Coulomb potential energy can be written as

$$U_{ii} = \sum_{j<j'}^{N_i} \frac{q_j q_{j'}}{r_{jj'}}, \tag{4}$$

where N_i is the number of ions, $r_{jj'} = |\mathbf{r}_j - \mathbf{r}_{j'}|$, and q_i is the total electric charge of an ion. In the RHS of Eq. (3), the second term $\mathbf{F}_{ie}$ corresponds to the response of background electrons to the ion dynamics.

Next, we assume the electronic response arises from two contributions, slow and fast, so that the resulting force $\mathbf{F}_{ie}$ can be split as

$$\mathbf{F}_{ie} = \mathbf{F}_{ie}^{\text{slow}} + \mathbf{F}_{ie}^{\text{fast}}, \tag{5}$$

where $\mathbf{F}_{ie}^{\text{slow}}$ contains forces that evolve on the slower ionic time scale to which the electrons can quickly react as a result of their much smaller mass. With this approximation, this instantaneous response can be included as screening of the ion-ion interactions; the electrons are considered to evolve implicitly with the ions [38]. With the addition of linear screening of ion-ion interactions [39,40], a modified Coulomb force $\mathbf{f}_{ii}$ can be written as

$$\mathbf{f}_{ii} = \mathbf{F}_{ii} + \mathbf{F}_{ie}^{\text{slow}}, \tag{6}$$

where $\mathbf{F}_{ii}$ is the Coulomb force without screening. The screened Coulomb (Yukawa) potential energy corresponding to $\mathbf{f}_{ii}$ can then be given as

$$U_{ii}^{\text{Ykw}}(t) = \sum_{j<j'}^{N_i} \frac{q_j q_{j'}}{r_{jj'}} e^{-r_{jj'}/\lambda_{\text{De}}(t)}. \tag{7}$$

It is important to note that the $U_{ii}^{\text{Ykw}}(t)$ continue to change during the evolution of the plasma because the electron Debye shielding length $\lambda_{\text{De}}(t)$ depends on time through the electron temperature $T_e(t)$ and the electron number density $n_e(t)$:

$$\lambda_{\text{De}}(t) = \sqrt{k_B T_e(t)/4\pi n_e(t) e^2}, \tag{8}$$

where k_B is the Boltzmann constant, and the electron number density $n_e(t)$ is the ratio of the total number of electrons N_e (fixed) to the occupied volume $\Omega_e(t)$ at a given time t, with

$$n_e(t) = N_e/\Omega_e(t). \tag{9}$$

The value of $\Omega_e(t)$ depends on the geometry of the system. The evolution of $T_e(t)$ is based on total-energy conservation, which is discussed below in this section.

The fast response of electrons is incorporated through a Langevin force [38]:

$$\mathbf{F}_{ie}^{\text{fast}} = -\gamma_{ie}(t) m_i \dot{\mathbf{r}}_j + \xi(t), \tag{10}$$

where γ_{ie} is the ion-electron collision frequency given by

$$\gamma_{ie}(t) = 1.6\times 10^{-9} n_e(t) \frac{m_p}{m_i} \frac{\ln\left(\sqrt{1+\Lambda_{ie}^2}\right)}{T_e^{3/2}(t)}, \tag{11}$$

where m_p is the proton mass. Here, we have replaced the standard Coulomb logarithm $\ln \Lambda_{ie}$ [41] with a modified form $\ln(\sqrt{1+\Lambda_{ie}^2})$ in order to guarantee that our Coulomb logarithm $\ln(\sqrt{1+\Lambda_{ie}^2}) \geqslant 0$. We estimate Λ_{ie} using a standard

Coulomb logarithm for electron-ion collisions [41]:

$$\ln \Lambda_{ie} = 23 - \ln\left[\sqrt{n_e(t)}T_e^{-3/2}(t)\right], \tag{12}$$

where Eq. (12) is solved for Λ_{ie}, which is the ratio of impact parameters in the collision; this Λ_{ie} value is then used in Eq. (11). In the RHS of Eq. (10), the first term is the dissipative frictional force, which causes the ions to slow, and the second term is the fluctuating force, which has zero mean ($\langle \xi(t)\rangle = 0$). Both of these terms are connected through the fluctuation-dissipation theorem [42], resulting in the variance $\langle \xi_j(t)\cdot\xi_l(t')\rangle = \sigma^2\delta_{jl}\delta(t-t')$; here, $\sigma^2 = 2k_B T_e(t)\gamma_{ie}(t)m_i$ ensures that the system converges toward the background electron temperature $T_e(t)$; δ_{jl} denotes a Kronecker delta; $\delta(t-t')$ denotes a Dirac delta, i.e., with no time correlation; and $\langle:\rangle$ indicates the average over noise realizations. (Note that the units are $\sigma^2 \sim \text{g}^2\,\text{cm}^2/\text{s}^3$.) Thus, in this system, the background electrons function as a heat bath for the ions.

The last term $\mathbf{F}_{in}$ in Eq. (3) incorporates the interactions between the ions and neutral atoms. In ion-neutral interactions, we treat an ion as a point charge that induces a dipole moment in a neutral atom, which causes this neutral atom to behave like an electric dipole [43–45]. Thus, ion-neutral interactions are a consequence of ion-dipole attraction [46,47]. We incorporate this term as a Langevin force, similar to Eq. (10):

$$\mathbf{F}_{in} = -\gamma_{in}(\mathbf{r})m_i\dot{\mathbf{r}}_j + \zeta(t). \tag{13}$$

Here, the spatial ion-neutral collision frequency $\gamma_{in}(\mathbf{r})$ is given as

$$\gamma_{in}(\mathbf{r}) = 2\pi q_i\sqrt{\frac{\alpha_n^p(m_i+m_n)}{m_i m_n}}\,n_n(\mathbf{r}), \tag{14}$$

where m_n is the mass of a neutral atom; $n_n(\mathbf{r})$ is the neutral number density, which varies spatially, depending on the configuration of the sculpted plasma; α_n^p is the polarizability of a neutral atom; and $\zeta(t)$ is the fluctuating force due to the neutral background. Again, both of the terms on the RHS in Eq. (13) satisfy the fluctuation-dissipation theorem, which ensures that the system converges toward the background neutral temperature $T_n = T_{i0}$, where T_{i0} is the initial ion temperature, and we assume that T_n remains constant during the simulation; the model could be improved to include the neutral temperature and momentum evolution as well.

Using Eqs. (2), (6), (10), and (13), we can write Eq. (3) as

$$m_i\ddot{\mathbf{r}}_j = \sum_{\substack{j'=1\\(j'\neq j)}}^{N} \mathbf{f}_{ii} - \gamma_{ie}(t)m_i\dot{\mathbf{r}}_j + \xi_j(t) - \gamma_{in}(\mathbf{r})m_i\dot{\mathbf{r}}_j + \zeta_j(t). \tag{15}$$

This is our equation of motion for the ions. In contrast to the usual Yukawa model, this model does not conserve energy as a result of the Langevin couplings to the electrons and neutrals, which we numerically find to be quite small, and as a result of the time dependence of the screening parameters.

We now examine our model's failure to conserve energy and seek a modification that will restore energy conservation. First, consider the total energy of the ions that yields the ionic forces in Eq. (15), that is, the sum of the ion kinetic, ion-ion potential, ion-neutral potential, and ion-electron potential energies. This total energy can be written as

$$\mathcal{E}_i(t) = K_i(t) + U_{ii}(t) + U_{ie}(t) + U_{in}(t), \tag{16}$$

where $U_{ii}(t)$ is time dependent; thus, $\mathcal{E}_i(t)$ is not conserved during the evolution of the nonequilibrium plasma. One way to conserve energy more appropriately is to modify the present model for an equilibrium plasma such that $U_{ii}(t)$ and λ_{De} are no longer time dependent, i.e., such that the background electron temperature and density are fixed. However, in nonequilibrium plasmas such as SUNPs, the background temperature and density vary during the evolution of the plasma, resulting in a mutual exchange of energy between ions and electrons that, in turn, affects the ion dynamics.

The total energy $\mathcal{E}_{\text{tot}}(t)$ at time t corresponding to our system in Eq. (1) is always conserved in reality and can be written as

$$\mathcal{E}_{\text{tot}}(t) = K_i(t) + K_e(t) + U_{ee}(t) + U_{ii}(t) + U_{ie}(t) + U_{in}(t). \tag{17}$$

Subtracting Eq. (16) from Eq. (17) at any time t and at $t = 0$, we obtain the following equations:

$$\mathcal{E}_{\text{tot}}(t) - \mathcal{E}_i(t) = K_e(t) + U_{ee}(t), \tag{18}$$

$$\mathcal{E}_{\text{tot}}(0) - \mathcal{E}_i(0) = K_e(0) + U_{ee}(0). \tag{19}$$

Now, subtracting Eq. (19) from Eq. (18), we obtain

$$\begin{aligned}\mathcal{E}_{\text{tot}}(t) - \mathcal{E}_{\text{tot}}(0) - \mathcal{E}_i(t) + \mathcal{E}_i(0)\\ = K_e(t) + U_{ee}(t) - K_e(0) - U_{ee}(0).\end{aligned} \tag{20}$$

Noting that $\mathcal{E}_{\text{tot}}(t) = \mathcal{E}_{\text{tot}}(0)$ because total energy is always conserved allows us to rewrite Eq. (20) as

$$\mathcal{E}_i(t) - \mathcal{E}_i(0) = -K_e(t) + K_e(0) - U_{ee}(t) + U_{ee}(0), \tag{21}$$

from which we can find the temperature

$$\begin{aligned}T_e(t) = \frac{2}{3N_e k_B}[U_{ee}(0) + K_e(0)\\ - U_{ee}(t) - \mathcal{E}_i(t) + \mathcal{E}_i(0)].\end{aligned} \tag{22}$$

We employ a simple interpolation for the electron potential energy that spans the weakly to strongly coupled regimes; this interpolation is of the form

$$U_{ee}(t) = -\frac{N_e e^2}{2}\frac{1}{\lambda_{\text{eff}}(t)}, \tag{23}$$

where $\lambda_{\text{eff}}(t) = \sqrt{\lambda_{\text{De}}^2(t) + [5a(t)/9]^2}$ can be interpreted as an effective screening length [17] for the electrons, and $a(t) = [4\pi n(t)/3]^{-1/3}$ is the usual ion-sphere radius (which varies in time because of density heterogeneities). Note that the weakly coupled energy is recovered when $a \ll \lambda_{\text{De}}$, so that

$$U_{ee}^w(t) \approx -\frac{N_e e^2}{2}\frac{1}{\lambda_{\text{De}}(t)}, \tag{24}$$

whereas, when $a \gg \lambda_{\text{De}}$, we recover the strongly coupled energy [48]

$$U_{ee}^s(t) \approx -\frac{9}{10}\frac{N_e e^2}{a(t)}. \tag{25}$$

Thus, Eq. (15) is coupled to Eq. (22), which is a nonlinear equation that we can solve with an iterative solver. All but one of the remaining terms in Eq. (22), namely, $U_{ee}(0)$, $K_e(0)$, and $\mathcal{E}_i(0)$, are given at $t = 0$ and will remain constant during simulation, while the term $\mathcal{E}_i(t)$ is updated during the simulation using Eq. (16). At each time step, the value of $T_e(t)$ is given and is considered an initial guess for the RHS of Eqs. (22) and (23); an updated value $T_e(t + \Delta t)$ at the next time step $t + \Delta t$ is then calculated as

$$T_e(t+\Delta t) = \frac{2}{3N_e k_B}[U_{ee}(0) + K_e(0) - U_{ee}(t) - \mathcal{E}_i(t) + \mathcal{E}_i(0)]. \tag{26}$$

The final electron temperature T_e^f is obtained using the following process:

$$T_e^f(t+\Delta t) = T_e(t+\Delta t)(1-\tau_0) + T_e(t)\tau_0. \tag{27}$$

The convergence of this scheme depends on the choice of the relaxation parameter τ_0; the optimal value of τ_0 is determined empirically [49]. In this way, energy conservation is now included in our model.

III. FIELD QUANTITIES FROM MD

As discussed above, SUNPs offer opportunities to study hydrodynamic phenomena, such as the perfect-fluid limit, closures, and kinetic phenomena. In this section, we formulate the microscopic variables of MD in terms of kinetic and hydrodynamic macroscopic variables that depend on both space and time to allow a nonequilibrium, heterogeneous plasma description. In addition, we develop local versions of the Coulomb coupling parameter and metrics for assessing deviations from equilibrium. The computational scheme for including spatial dependencies is discussed in Sec. III.

The phase-space evolution of the ions is described by the Klimontovich distribution function

$$\mathcal{N}(\mathbf{r},\mathbf{v},t) = \sum_{j=1}^{N_i} \delta[\mathbf{r}-\mathbf{r}_j(t)]\delta[\mathbf{v}-\mathbf{v}_j(t)], \tag{28}$$

from which we can compute various moments

$$\mathcal{M}^\alpha(\mathbf{r},t) = \int d\mathbf{v}\, \mathbf{v}^\alpha \mathcal{N}(\mathbf{r},\mathbf{v},t), \tag{29}$$

where α is the order of the moment. The three basic hydrodynamic moments can be computed with $\alpha = 0, 1, 2$. First, the ion number density $n_i(\mathbf{r}, t)$ (zeroth-order moment, $\alpha = 0$) is

$$n_i(\mathbf{r},t) = \sum_{j=1}^{N_i} \delta[\mathbf{r}-\mathbf{r}_j(t)]. \tag{30}$$

Next, the bulk flow $\mathbf{u}_i(\mathbf{r}, t)$ (first-order moment, $\alpha = 1$) is given by

$$\mathbf{u}_i(\mathbf{r},t)n_i(\mathbf{r},t) = \sum_{j=1}^{N_i} \mathbf{v}_j(t)\delta[\mathbf{r}-\mathbf{r}_j(t)]. \tag{31}$$

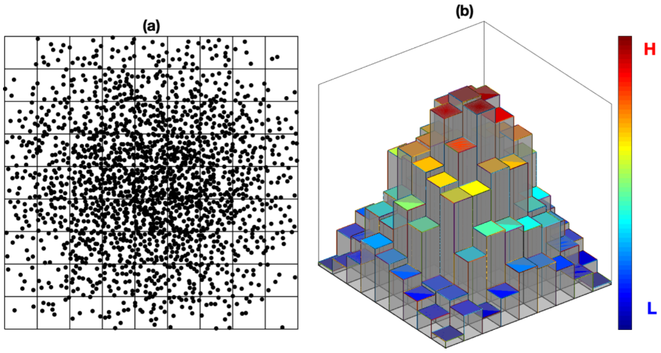

FIG. 1. Coarse-graining procedure. We obtained field quantities from the MD particle positions through coarse-graining physical quantities on a mesh; an example of a two-dimensional Cartesian mesh is shown in the left panel (a). The figure on the right, panel (b), shows the coarse grained density associated with the MD data shown on the left, where the color scale indicates higher (H) and lower (L) densities [58]. Meshes in other dimensions and coordinate systems were also used.

Lastly, the ion temperature $T_i(\mathbf{r}, t)$ (second-order moment, $\alpha = 2$) is given by

$$\frac{3k_B T_i(\mathbf{r},t)}{m_i} n_i(\mathbf{r},t) = \sum_{j=1}^{N_i} [\mathbf{v}_j(t) - \mathbf{u}_i(\mathbf{r},t)]^2 \delta[\mathbf{r}-\mathbf{r}_j(t)]. \tag{32}$$

These hydrodynamic moments, obtained directly from MD, are exact because they are definitions that directly employ the particle trajectory information. This is in contrast to theoretical approaches in which the coupled equations of motion for the moments require an approximate closure; thus, deviations from theoretical predictions that are seen in the MD can suggest areas where SUNPs can potentially reveal information about kinetic theory closures.

The above expressions for the moments can be formally defined, but they do not correspond to the smooth, ensemble-averaged quantities employed in kinetic theory and hydrodynamics. Thus, based on the symmetry of a system, we locally coarse-grained the different field quantities in cylindrical or Cartesian coordinates. A schematic picture of a coarse-grained mesh in Cartesian coordinates is illustrated in Fig. 1. The coarse-graining procedure involves decomposing space into a grid, which is typically chosen to be consistent with the symmetries of the plasmas (and therefore a specific coordinate system). The grid spacing is chosen to balance the ability to resolve important gradients with the ability to yield a reasonable average.

We can also define other field variables for SUNPs. Of interest for nonideal plasmas is the unscreened Coulomb coupling parameter $\Gamma_i(\mathbf{r}, t)$, which is readily generalized to have spatiotemporal variations:

$$\Gamma_i(\mathbf{r},t) = \frac{q_i^2}{a_{WS}(t)} \frac{1}{k_B T_i(\mathbf{r},t)} = \left(\frac{4}{3}\pi n_i(\mathbf{r},t)\right)^{1/3} \frac{q_i^2}{k_B T_i(\mathbf{r},t)}. \tag{33}$$

This function reveals locations in the plasma with stronger or weaker coupling and can suggest phase-space manipulations

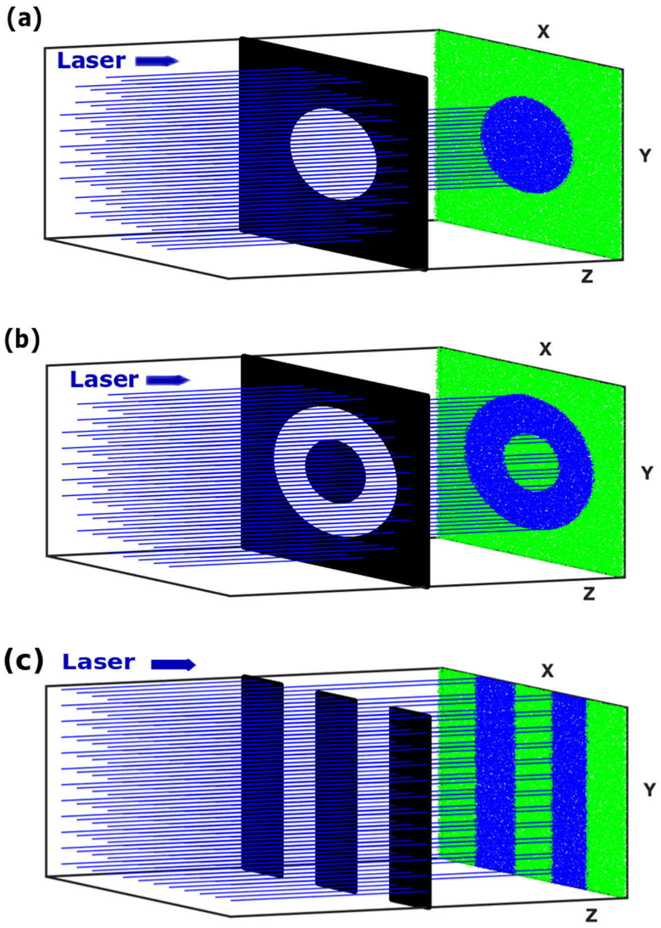

FIG. 2. Formation of a SUNP. We illustrate the creation of a sculpted plasma using a mask. The laser radiation is incident from the left and partially blocked by the mask, which is shown in black. A portion of the radiation reaches the cold gas, which is near the green plane, and that portion is photoionized (blue portion). Solid-rod, hollow-rod, and gapped-slab plasmas are shown in (a), (b), and (c), respectively.

(e.g., evaporation) that could allow us to design plasmas with custom coupling profiles.

In addition, we wish to know which regions of the plasma are in local equilibrium (local Maxwellian) or are kinetic (deviating from a local Maxwellian) and whether we can control how "kinetic" the system is. Field variables that serve as relevant metrics are the dimensionless moment ratios $\beta_1(\mathbf{r},t)$ and $\beta_2(\mathbf{r},t)$ [9,50] of the distribution function, which we define as

$$\beta_1(\mathbf{r},t) = \frac{\left\langle \sum_{j=1}^{N_i} [\mathbf{v}_j(t) - \mathbf{u}_i(\mathbf{r},t)]^4 \delta[\mathbf{r} - \mathbf{r}_j(t)] \right\rangle}{\left\langle \sum_{j=1}^{N_i} [\mathbf{v}_j(t) - \mathbf{u}_i(\mathbf{r},t)]^2 \delta[\mathbf{r} - \mathbf{r}_j(t)] \right\rangle^2}, \tag{34}$$

$$\beta_2(\mathbf{r},t) = \frac{3}{5}\frac{\left\langle \sum_{j=1}^{N_i} [\mathbf{v}_j(t) - \mathbf{u}_i(\mathbf{r},t)]^6 \delta[\mathbf{r} - \mathbf{r}_j(t)] \right\rangle}{\left\langle \sum_{j=1}^{N_i} [\mathbf{v}_j(t) - \mathbf{u}_i(\mathbf{r},t)]^2 \delta[\mathbf{r} - \mathbf{r}_j(t)] \right\rangle^3}. \tag{35}$$

Here, $\langle X \rangle$ represents a quantity that has been coarse-grained using the procedure shown in Fig. 1. These moment ratios have been designed to be unity when the distribution function is consistent with a drifting Maxwell-Boltzmann distribution; that is, the plasma is near local thermodynamic equilibrium. Note that $\beta_1(\mathbf{r},t)$ and $\beta_2(\mathbf{r},t)$ employ different moments; β_2 has the highest-order moment and is thus more sensitive to deviations in the tail of the distribution.

IV. HYDRODYNAMICS MODEL IN THE PERFECT-FLUID LIMIT

The degree of control over the Coulomb coupling parameter allowed by UNP experiments translates into control over expansion parameters in kinetic theory, such as the Knudsen number [51]. Such control suggests that UNPs are an ideal platform for exploring hydrodynamic closures. In particular, there has recently been interest in "perfect fluids," mainly in the contexts of quark-gluon plasmas [52] and dense plasmas [53]; in such fluids, the mean free path is near its minimum, a limit in which there is essentially no transport, and the Euler form of hydrodynamics is nearly exact. UNPs appear to be the most natural platform for exploring the physics of perfect fluids both because the experiments are well characterized (e.g., with well-known density, temperature, and ionization state) and because the transport coefficients are very small or near their minima [17]. Here, we review a standard approach to hydrodynamics in the perfect-fluid limit, which yields a quantity that can be used as a metric for a perfect fluid (that is, a fluid with the smallest possible viscosity).

We begin with the Euler hydrodynamic equations for the nonviscous flow of a gas:

$$\frac{\partial \rho_i}{\partial t} + \nabla\cdot(\rho_i \mathbf{u}_i) = 0, \tag{36}$$

$$\left(\frac{\partial}{\partial t} + \mathbf{u}_i\cdot\nabla\right)\mathbf{u}_i + \frac{1}{\rho_i}\nabla\cdot P_i = \frac{\mathbf{F}_m}{m_i}, \tag{37}$$

$$\left(\frac{\partial}{\partial t} + \mathbf{u}_i\cdot\nabla\right)T_i + \frac{2}{3}(\nabla\cdot\mathbf{u}_i)T_i = 0, \tag{38}$$

where $\rho_i = m_i n_i$, and $\mathbf{F}_m$ is the mean-field force. This particular form of the hydrodynamics equations arises from the assumption that the phase-space distribution is very close to a Maxwell-Boltzmann distribution $\mathcal{F}_{\mathrm{MB}}(\mathbf{r},\mathbf{v},t)$, as a result of the high collisionality, and yields a simple scalar pressure and no heat flux ($\mathbf{Q}_i = 0$).

Equations (36) and (38) may be rewritten as

$$\left(\frac{\partial}{\partial t} + \mathbf{u}_i\cdot\nabla\right)\rho_i = -\rho_i\nabla\cdot\mathbf{u}_i, \tag{39}$$

$$-\frac{3}{2}\frac{\rho_i}{T_i}\left(\frac{\partial}{\partial t} + \mathbf{u}_i\cdot\nabla\right)T_i = \rho_i\nabla\cdot\mathbf{u}_i. \tag{40}$$

Adding these two equations together, which cancels the terms on the RHSs, we obtain

$$\left(\frac{\partial}{\partial t} + \mathbf{u}_i\cdot\nabla\right)\rho_i - \frac{3}{2}\frac{\rho_i}{T_i}\left(\frac{\partial}{\partial t} + \mathbf{u}_i\cdot\nabla\right)T_i = 0, \tag{41}$$

which can be rewritten as

$$\left(\frac{\partial}{\partial t} + \mathbf{u}_i\cdot\nabla\right)\left(\rho_i T_i^{-3/2}\right) = 0. \tag{42}$$

This well-known result predicts that the quantity $\rho_i/T_i^{3/2}$ is constant along streamlines, an evolution known as an adiabatic transformation for a perfect fluid.

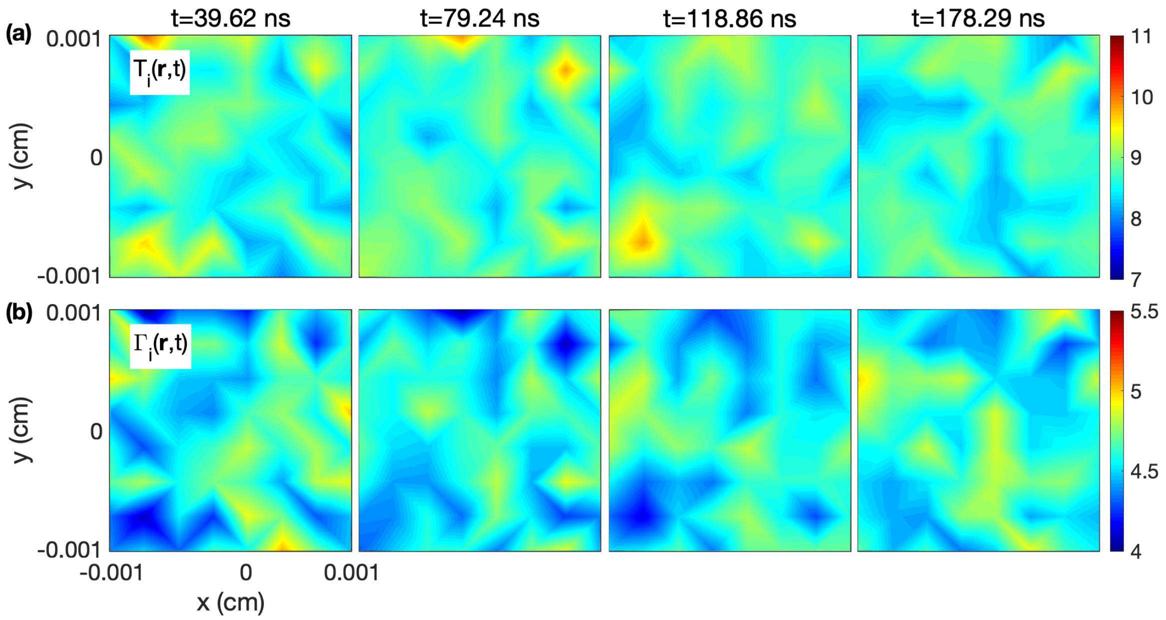

FIG. 3. Evolution of field quantities of a reference plasma. The coarse-grained (a) ion temperature $T_i(\mathbf{r},t) \approx 9$ K and (b) ion coupling parameter $\Gamma_i(\mathbf{r},t) \approx 5$ are shown. Note that we can observe local fluctuations in these field quantities even in the homogeneous, periodic case.

Consider the case in which the field variables are linearized around their uniform values. Equation (42) then becomes

$$\frac{3}{2}\rho_i\frac{\partial T_i}{\partial t} - T_i\frac{\partial \rho_i}{\partial t} = 0. \tag{43}$$

Note that in this limit the spatial gradient vanishes, and the equation is readily integrated; we thus obtain

$$n_i(t) = n_{i0}\left(\frac{T_i(t)}{T_{i0}}\right)^{3/2}. \tag{44}$$

This relation implies that, under the assumptions made, $n_i(t)T_i(t)^{-3/2}$ is constant *everywhere*. Thus, when $n_i(t)T_i(t)^{-3/2} = \mathcal{C}$, the UNP dynamics should be those of a perfect fluid; this condition is readily observed in the MD simulations, as discussed below.

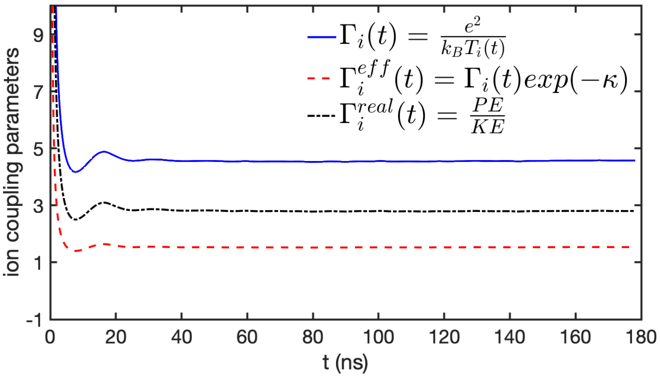

FIG. 4. Time evolution of the ion coupling parameter for a reference plasma. The unscreened ion coupling parameter $\Gamma_i(t) \approx 5$ (–), the effective ion coupling parameter $\Gamma_i^{\rm eff}(t) = \Gamma_i \exp(-\kappa) \approx 1.5$ (–), and the real ion coupling parameter $\Gamma_i^{\rm real}(t) = PE/KE$ (---) are shown.

V. SIMULATION METHODS AND RESULTS

We now turn to the NEMD computational procedure for studying SUNPs and then present the results of our studies. Experimentally, the ionizing beam is incident on a mask, with spatial variations in transmissibility, and the transmitted radiation is allowed to ionize the ultracold atoms [30,31]. In Figs. 2(a), 2(b), and 2(c), we illustrate this strategy for the three examples of a solid rod, a hollow rod, and a gapped slab, respectively.

All simulations were performed using the LAMMPS package [54] with a simulation time step $\Delta t = 0.01\omega_i^{-1}$ s in the microcanonical ensemble. In all cases, the SUNP was taken to be singly ionized strontium (Sr$^+$), with $m_i = 14.55\times10^{-23}$ g, an initial temperature of $T_{i0} = 1.0$ mK, and a polarizability $\alpha_p = 25\times10^{-24}$ cm^3 [55]. The electron density $n_e(t)$ and temperature $T_e(t)$ were updated at each time step according to Eqs. (9) and (22), respectively; those updates indirectly impact all other parts of the model, including the Langevin parameters and the electron screening length $\lambda_{\rm De}(t)$, in accordance with Eq. (8). The relaxation parameter in (27) was fixed at $\tau_0 = 0.5$ in all simulations. Other parameters were chosen according to the specific geometry of the initial configuration. The different field quantities were calculated after disorder-induced heating was allowed to occur.

A. Homogeneous, nonsculpted UNP: Reference case

We first discuss a reference case, which is the often-studied homogeneous plasma. Understanding the homogeneous case allows us to determine the impacts of heterogeneities. For example, it is of interest to know whether Coulomb coupling can be controlled (e.g., increased) in SUNPs relative to this reference case. Thus, we begin by considering a periodic, nonsculpted UNP system with no neutral atoms, i.e., $\gamma_{in} = 0$. The Sr$^+$ was taken to have a density of $n_{i0} = 3.197\times10^{12}$ cm^{-3}

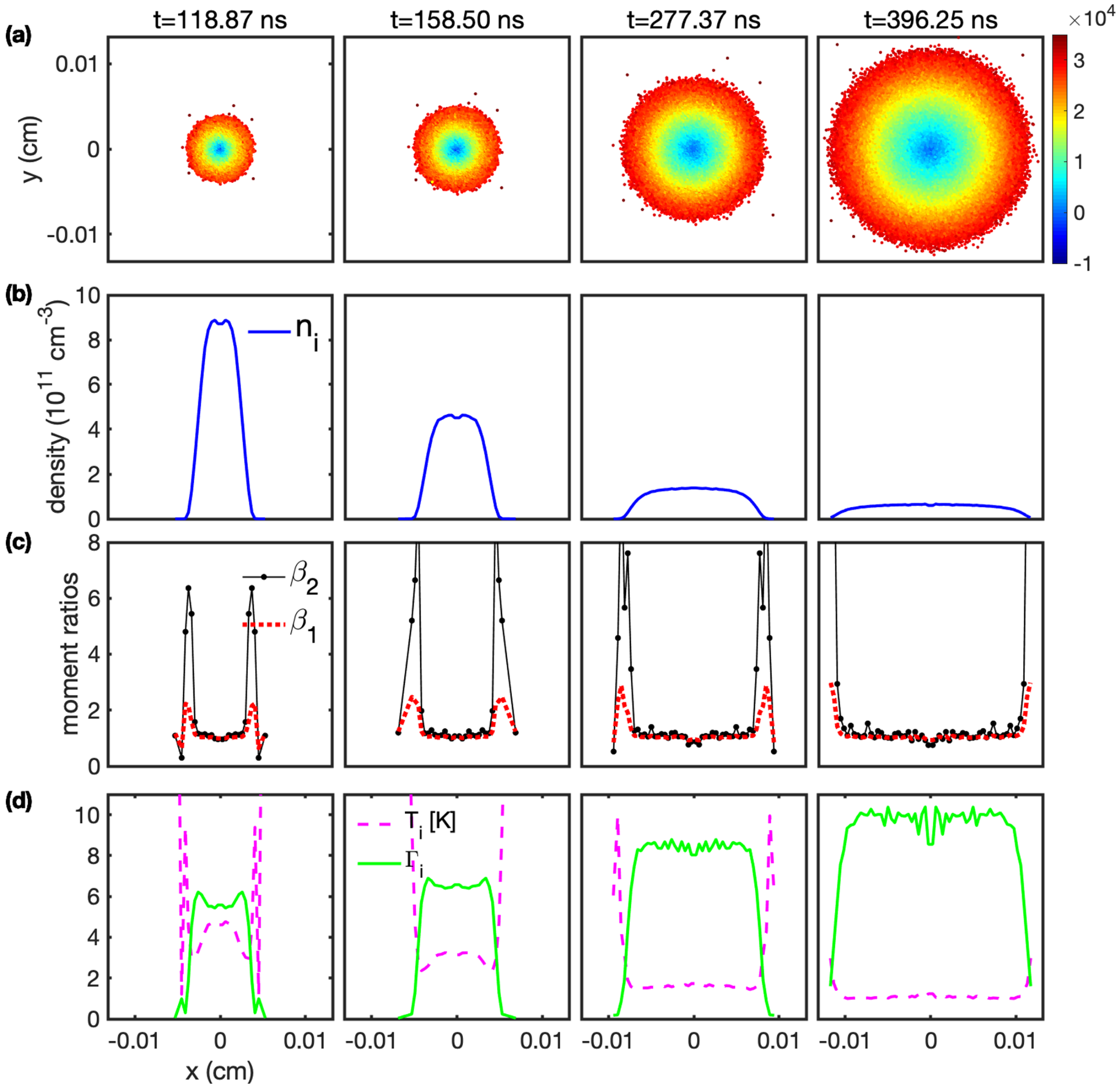

FIG. 5. Evolution of a solid-rod SUNP and several radial field quantities. In (a), the time evolution of an initially cylindrical plasma is shown in physical space; the colorbar indicates the radial velocity. The line plots in (b), (c), and (d) show the corresponding radial field quantities. In (b), the ion density $n_i(r,t)$ (–) is shown. In (c), the ion moment ratios $\beta_1(r,t)$ (...) and $\beta_2(r,t)$ (-•-) are shown. In (d), the ion temperature $T_i(r,t)$ (- -) and the ion coupling parameter $\Gamma_i(r,t)$ (–) are shown. Note that both of the β fields are nearly unity in the center of the plasma, where the coupling is higher, indicating that near-equilibrium conditions are obtained in the central region; in contrast, a more kinetic plasma ($\beta \gg 1$) is seen at the periphery.

within a cubical box with sides of length 2.3×10^{-3} cm. We held the electron temperature constant at $T_{e0} = 100$ K and the electron density constant at $n_{e0} (= n_{i0})$ for these simulations. All other parameters were the same as discussed above.

The contour plots in Fig. 3(a) confirm that temperatures $T_i(\mathbf{r},t)$ throughout the plasma maintained a value of ≈9 K and changed little over time. Similarly, Fig. 3(b) shows that the value of $\Gamma_i(\mathbf{r},t)$ stayed constant at ≈5, as expected. Also, a comparison between Figs. 3(b) and 4 (solid line) makes it clear where $\Gamma_i(t) \approx 5$ as well. It is pertinent to mention that the effective/screened ion coupling parameter $\Gamma_i^{\text{eff}}(t)$ for a Yukawa potential is defined as $\Gamma_i^{\text{eff}}(t) = \Gamma_i(t)\exp(-\kappa)$, given $\Gamma_i(t)$ and the screening parameter $\kappa = a_{aw}/\lambda_{\text{De}}$. As shown in Fig. 4 (dotted line), the value of $\Gamma_i^{\text{eff}}(t)$ for $\kappa = 1.091$ is ≈1.5 after disorder-induced heating, as predicted [56,57].

From these simulations of a nonsculpted UNP, we thus obtain reference values for plasma parameters, holding $(T_i(\mathbf{r},t), \Gamma_i(\mathbf{r},t)) \approx (9\text{ K}, 5)$, and we will compare our results for SUNPs to these reference values.

B. Solid-rod SUNP: Expansion phenomenon

Perhaps the simplest sculpted plasma is one in which the laser is masked to form a sharp outer edge around an otherwise quasiuniform cross section (see Supplemental Material [58]). A plasma formed from such an arrangement, shown in Fig. 2(a), has the shape of a solid rod. We explored this geometry with a plasma of radius $r_0 = 1\times10^{-3}$ cm ($t = 0$) centered on the z axis and bounded by the surfaces $z = -1\times10^{-3}$ and 1×10^{-3} cm. An open boundary in the x-y plane and a periodic boundary condition in the z direction

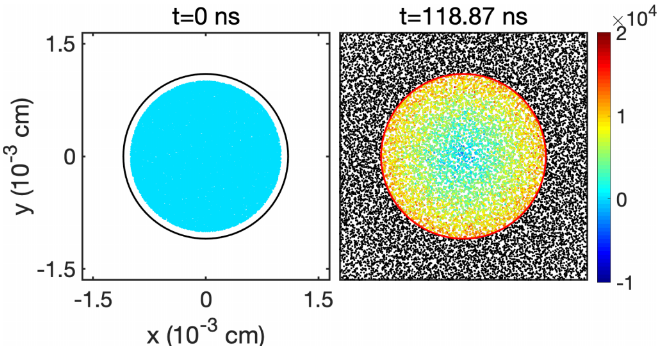

FIG. 6. The cross section of a cylindrical volume of radius $1.1r_0$ over which the different transport quantities are calculated for a solid-rod SUNP (shown below in Fig. 7). The left snapshot shows the plasma at the initial time $t = 0$, and the right snapshot shows the plasma at $t = 118.87$ ns, when the plasma starts to expand in hydrodynamic fashion. The boundary of the volume element is shown with a red circle. The colorbar indicates the radial velocity inside the volume-element boundary, and the plasma particles outside the boundary are shown with black dots (without any corresponding scale).

were used. The initial electron temperature was $T_{e0} = 100$ K, and the initial electron density n_{e0} and ion density n_{i0} were $n_{e0} = n_{i0} = 3.197\times 10^{12}$ cm^{-3}. During this radial expansion, the Sr$^+$ ions collide with the surrounding static, neutral Sr atoms, with spatial variation

$$n_n(r) = n_{n0}\left(1 - \frac{1}{1 + \exp[c_0(r - r_{\text{edge}})]}\right), \qquad (45)$$

where n_{n0} is the neutral density at $t = 0$, $c_0 = 1\times 10^4$ cm^{-1} is a parameter to control the width of the transition from the ionized region to the nonionized region, and $n_n(r)$ causes the change in the ion-neutral collision frequency $\gamma_{in}(\mathbf{r})$ [see Eq. (14)].

A summary of the dynamics observed in our simulation is shown in Fig. 5. Our main interests are to determine whether various hydrodynamic regions form, as defined through our kinetic parameters, and whether the local coupling increases because of the local loss of fast particles. From the top row to the bottom row, we show the expansion of the plasma in physical space with color coding by plasma particle velocities [Fig. 5(a)], the radial density [Fig. 5(b)], the moment ratios $\beta_1(\mathbf{r},t)$ and $\beta_2(\mathbf{r},t)$ [Fig. 5(c)], and the field quantities $T_i(\mathbf{r},t)$ and $\Gamma_i(\mathbf{r},t)$ [Fig. 5(d)]. The moment ratios reveal that the outer portions of these plasmas are quite kinetic, with very hydrodynamic regions in the interior. That values of the radial velocity are negative near the center and higher near the edges suggests that fast particles are moving through the plasma, eventually leaving behind lower-velocity particles. (This phenomenon is more dramatic in the hollow-rod geometry discussed in the next subsection.) Overall, the edges are hotter, and the central region does, in fact, cool; the interior temperature is substantially lower than the temperature $T_i \approx 9$ K observed for the nonsculpted plasma case. Also, both of the β fields are nearly unity in this central region. Thus, the central region of a solid-rod-shaped SUNP is relatively cooler, which increases the coupling and makes the plasma more collisional; the plasma in this region also behaves as a perfect fluid, as it satisfies the adiabatic condition that resulted from the Euler hydrodynamic model. Our model predicts couplings as high as $\Gamma_i(r,t) \approx 10$, which is comparable to the largest coupling achieved in any published experiment to date [59].

We performed a test to establish the late-time (well after disorder-induced heating has occurred) thermodynamic state of the inner region (defined in terms of an integral over the inner shells); we found that this region exhibits adiabatic cooling according to $n_i(t)T_i(t)^{-3/2} = n_{i0}T_{i0}^{-3/2}$. This suggests that this inner region exhibits Euler-like hydrodynamics, consistent with the high values of Coulomb coupling that the model predicts.

Other "region-averaged" quantities were computed, according to the scheme shown in Fig. 6; Fig. 7 shows various quantities that depend only on time. Figures 7(a) and 7(b) show the temporal decay of ion density and ion temperature, respectively. The temporal evolutions of the moment ratios β_1 and β_2 are shown in Fig. 7(c); the values of both of these moments remain at ≈1. In Figs. 7(a) and 7(b), solid lines are

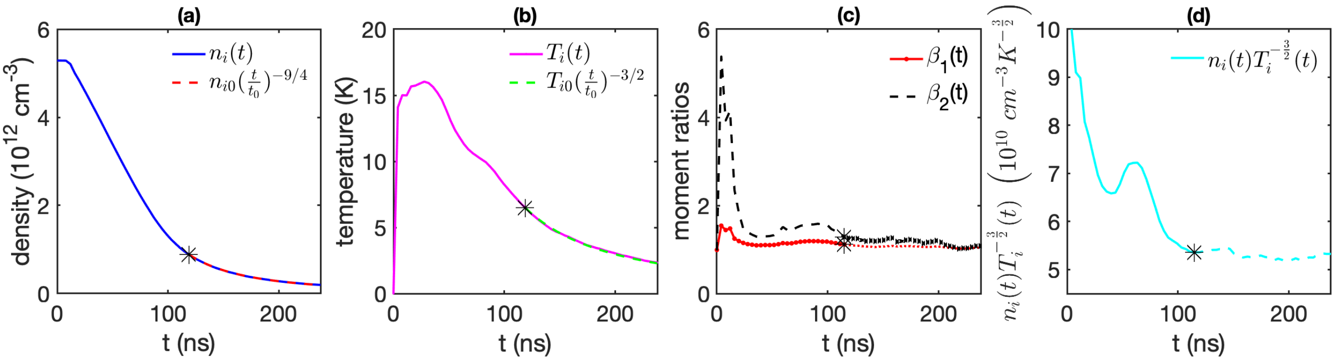

FIG. 7. The evolution of several spatially averaged quantities of a solid-rod SUNP (see Fig. 6) of radius $1.1r_0$. The temporal evolution of (a) ion density, (b) ion temperature, (c) moment ratios, and (d) the quantity in (6) is shown. The panels (c) and (d) indicate that the plasma is largely hydrodynamic at later times, which is indicated by a star in all of the plots ($t > 118.87$ ns). This is confirmed in panels (a) and (b) by fitting (dashed lines) the late time behavior to the hydrodynamic prediction, and the fit is excellent. Taken together, these results indicate how and when the plasma approaches a well-defined hydrodynamic state, following a kinetic phase during and after DIH.

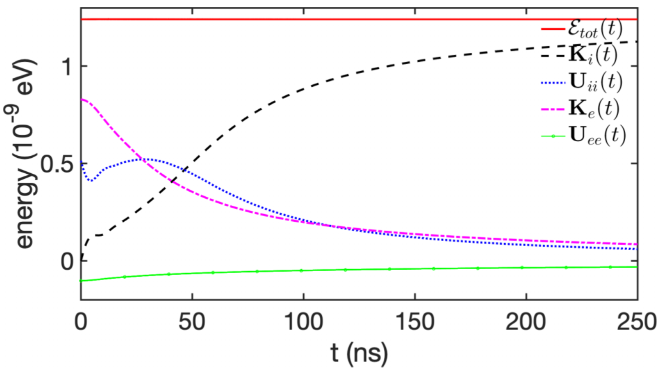

FIG. 8. Total-energy conservation $\mathcal{E}_{\text{tot}}(t)$, given by Eq. (17), for a solid-rod SUNP. All of the line plots are given except those for the terms $U_{ie}(t)$ and $U_{in}(t)$.

used to indicate the MD results, and the dotted lines show the following relations:

$$n_i(t) = n_{i0}\left(\frac{t}{t_0}\right)^{-9/4}, \tag{46}$$

$$T_i(t) = T_{i0}\left(\frac{t}{t_0}\right)^{-3/2}, \tag{47}$$

where $t \geqslant t_0$, and n_{i0} and T_{i0} are the constant initial ion density and ion temperature, respectively, at time $t_0 = 118.87$ ns. Finally, Eq. (46) can be combined with Eq. (47) to obtain the following relation between ion density and ion temperature:

$$n_i(t) = n_{i0}\left(\frac{T_i(t)}{T_{i0}}\right)^{3/2}. \tag{48}$$

This relation implies that $n_i(t)T_i(t)^{-3/2} = n_{i0}T_{i0}^{-3/2}$, i.e., that this quantity should remain constant. Figure 7(d) shows the temporal evolution of $n_i(t)T_i^{-3/2}(t)$ (shown as a cyan line), which eventually maintains a constant value of $\approx 5.4\times10^{10}$ over time (the dashed portion). Here, the time evolution of this relation exhibits a spiky behavior, which can be avoided by taking the ensemble average of $\langle n_i(t)T_i^{-3/2}(t)\rangle$ over several repeated experiments and simulations.

For each of the sculpted cases, we examined the overall energy balance based on the model. For this geometry, the energy budgets are shown in Fig. 8. Our overall energy is conserved (by construction), with the largest changes occurring in the kinetic energy of the ions. The sources of this energy are primarily electron cooling and a decrease in the ion potential energy. This is somewhat analogous to disorder-induced heating, although here much of the ionic kinetic energy is in bulk hydrodynamic flow.

C. Hollow-rod SUNP: Implosion and expansion processes

Next, we consider a simple hollow-rod SUNP formed by a mask as shown in Fig. 2(b) [58]. The time evolution of such a hollow-rod SUNP is shown in Fig. 9 at four time points. The first panel of Fig. 9 shows the plasma at $t = 0$, with initial electron and ion densities of $n_{e0} = n_{i0} = 6.261\times10^{11}$ cm^{-3} within a cylindrical shell of inner radius $r_{\text{inner}} = 1.5\times10^{-3}$ cm, outer radius $r_{\text{outer}} = 2.5\times10^{-3}$ cm, and length along the z direction of 2×10^{-3} cm. The neutral density $n_n(r)$ is given by

$$n_n(r) = n_{no}\left[1 - \frac{1}{1+\exp[c_o(r - r_{\text{outer}})]} + \frac{1}{1+\exp[c_o(r - r_{\text{inner}})]}\right], \tag{49}$$

where $c_o = 1\times10^5$ cm^{-1}. All other parameters are the same as for the solid-rod SUNP discussed above. An open boundary condition in the x-y plane and a periodic boundary condition in the z direction were used. Color intensity corresponds to the radial velocity. Unbalanced electric fields accelerate ions on the inner and outer boundaries, as can be seen in the second panel. The implosion dynamics in the inner region generates a strong energy source, in the form of high density and temperature, along the axis of the hollow-rod plasma. In the final panel of Fig. 9, we see that this energy source, in turn, causes an explosion, which results in the formation of a cylindrical blast wave moving outward through the expanding plasma.

Details of the expansion dynamics for the hollow plasma, along with other field quantities, are shown for later times in Fig. 10, in order to determine the nature of the blast wave [58]. Figure 10(a) shows the late-time density distribution, and Fig. 10(b) shows the cross section of the density. In the inner region, the plasma is very uniform in all of its quantities, including the kinetic moments, shown in Fig. 10(c), and the temperature and coupling, shown in Fig. 10(d). Perhaps

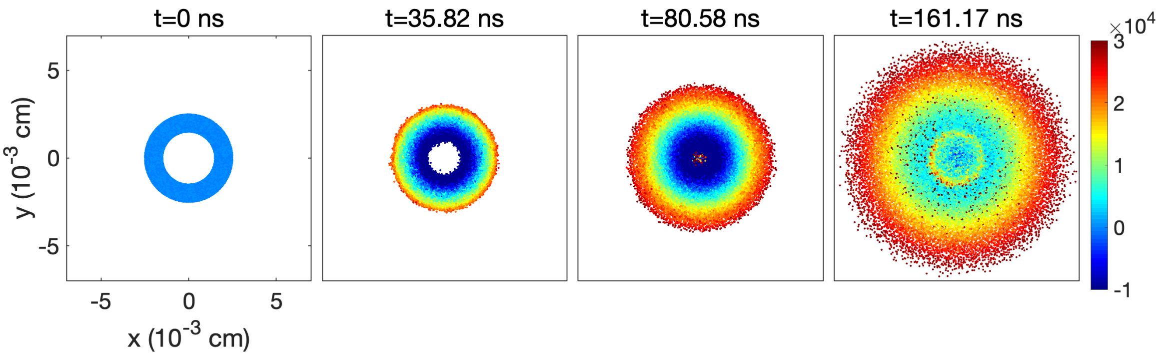

FIG. 9. Evolution of a hollow-rod SUNP. Time moves forward from the left panel to the right panel. The radial velocity is indicated by the colorbar; note the explosion in the outer region and the implosion that fills the hollow region. At late times, the imploding particles cross the central axis and create an outgoing wave, as can be seen in the rightmost panel.

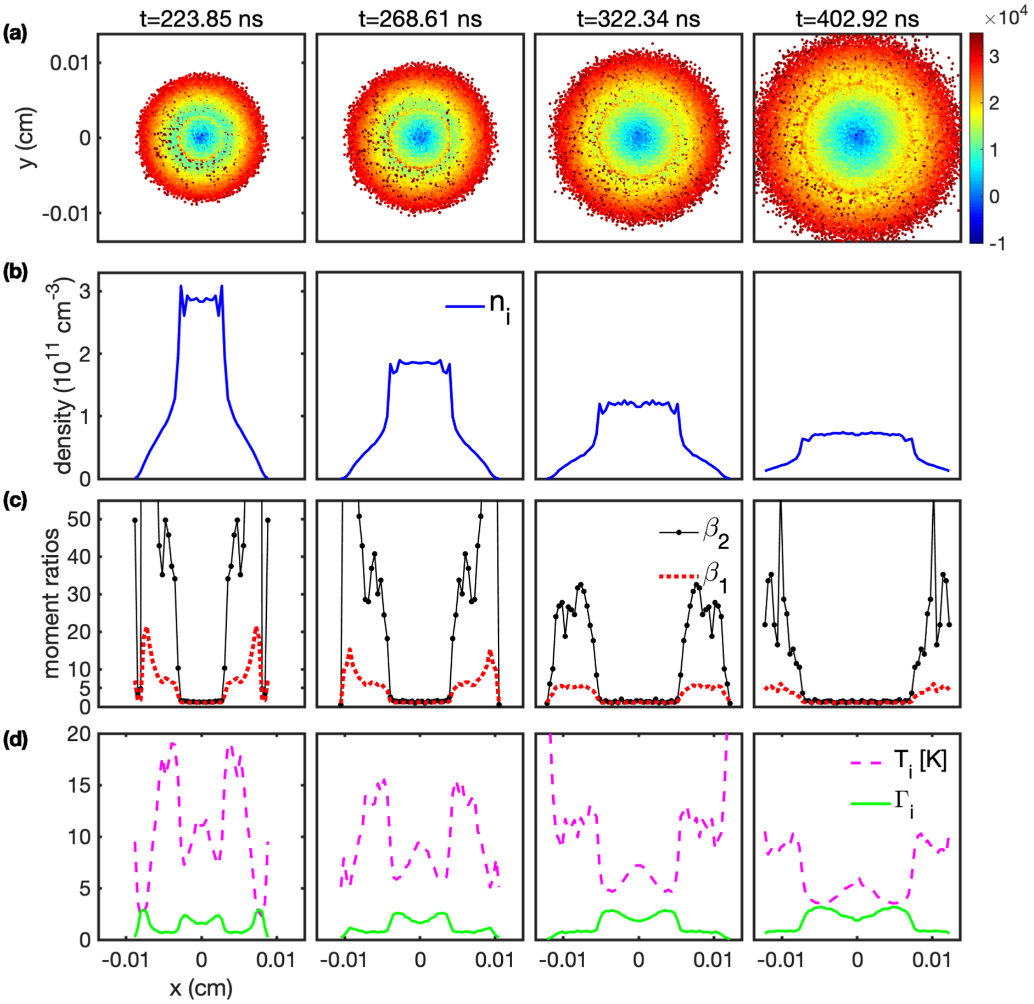

FIG. 10. Late-time evolution of a hollow-rod SUNP. MD particles, representing the density $n_i(\mathbf{r}, t)$, are shown in row (a) as points colored to indicate their radial velocities. Note that an outgoing wave is seen, created by fast particles that have passed through the center. In row (b), we analyze the conditions of this shocklike structure in more detail with a radial density. Interestingly, these results reveal that this nonlinear wave does not exhibit the usual form of a shock, but rather a type of "inverted shock": the temperature $T_i(\mathbf{r}, t)$ (– –) is larger *in front* of the wave and the coupling $\Gamma_i(\mathbf{r}, t)$ (—) is higher *behind* the wave. The moment ratios $\beta_1(\mathbf{r}, t)$ (· · ·) and $\beta_2(\mathbf{r}, t)$ (-·-) are unity behind the moving wave, but a very kinetic plasma is seen in front of the wave. However, the density shown in row (b) is shocklike, with a constant, higher density behind the wave.

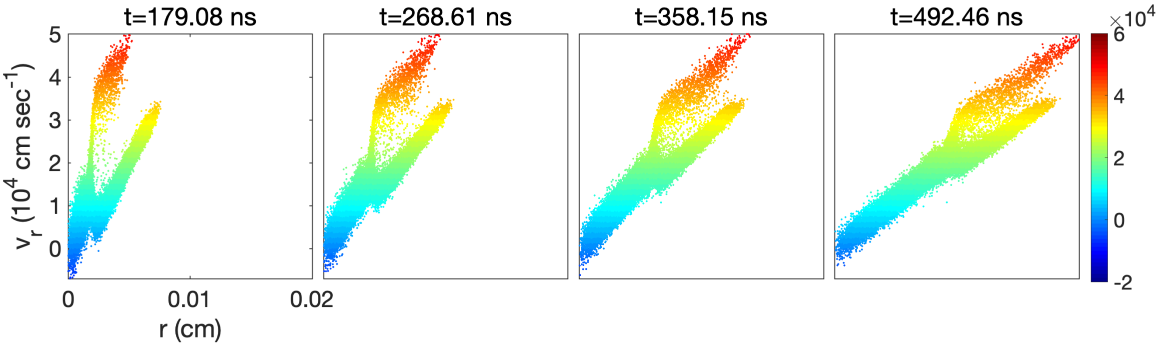

FIG. 11. Late time evolution of a hollow-rod SUNP in phase space. The phase-space evolution of a hollow-rod plasma is shown, revealing the role of imploding particles (with negative radial velocity) as they pass through the origin and create an outgoing wave. The imploding particles, which have been accelerated as they approach the origin, are a fast beam that overtakes the remaining plasma. The phase-space view of this process reveals why the outgoing wave differs from a typical shock wave.

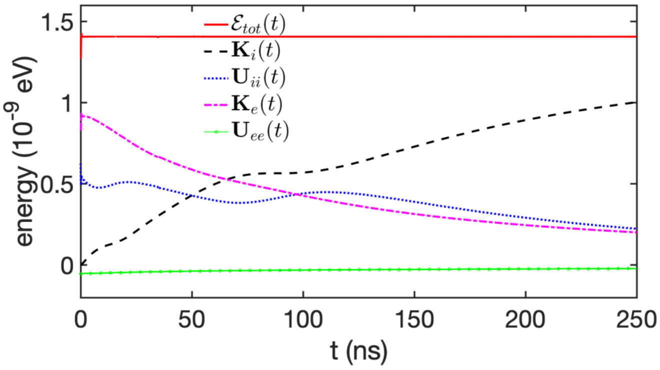

FIG. 12. Total-energy conservation $\mathcal{E}_{\rm tot}(t)$, given by Eq. (17), for a hollow-rod SUNP. All of the line plots are given except those for the terms $U_{ie}(t)$ and $U_{in}(t)$.

surprisingly, this implosion dynamics leads to a very uniform and quiescent strongly coupled plasma; further engineering of the "inverse problem" of producing desired conditions at late times could yield improvements. In contrast with the inner region of the plasma, the outer region is characterized by an outward blast wave moving through a hotter, locally kinetic outer layer. Such wave properties have been observed and studied previously [60–66].

The late time expansion of the plasma in phase space is shown in Fig. 11. Note that the ions that imploded on the central axis are moving outward at much higher velocities than are those from the outer boundary, as can be seen by the high-velocity branch of the plot. Thus, the acceleration inward experienced by particles initially in the inner region is larger than the acceleration outward experienced by particles initially on the outer surface of the plasma, and the fast particles pass through the plasma and overtake the rest of the plasma; such a configuration could be used to study, for example, instabilities such as the Kelvin-Helmholtz instability. However, we also see in phase space that there is a region of plasma near $r = 0$ where the velocity is near zero; this region is the near-uniform, quiescent plasma discussed above. This dynamics can also be seen in Fig. 12, where the energy budgets are shown. A large increase in the ion kinetic energy is shown, which initially comes from the kinetic energy of the electrons, but later comes from the potential energy of the ions. Compared with the other geometries we explore in this paper, this hollow-rod plasma configuration is notable for its creation of both fast ions and a near-uniform, quiescent inner region.

D. Gapped-slab SUNP: Beam formation

Next, we consider a gapped-slab SUNP, defined as a plasma slab with a portion removed in the center, as shown in Fig. 13(a). The gap arises from a rectangular mask, shown schematically in Fig. 2; thus, the gap initially contains only neutrals. The goal of this geometry is to explore plasmas with relative drift (as in strongly coupled beams [67,68]), fluid instabilities (such as Kelvin-Helmholtz [69,70] and Rayleigh-Taylor [71] instabilities), two-stream [72–74] and bump-on-tail [75] instabilities, and stopping-power [76–78] geometries. The geometry of the gapped-slab SUNP studied here is shown in Fig. 13. The simulation box is defined as follows: y and z range from -0.5×10^{-3} to 0.5×10^{-3} cm, and x ranges from -2.25×10^{-3} to 2.25×10^{-3} cm with a gap from -1.25×10^{-3} to 1.25×10^{-3} cm, so that the width of the gap is $g_w = 2.5\times10^{-3}$ cm. The initial electron temperature is $T_{e0} = 100$ K, and the initial electron/ion density is $n_{e0}(= n_{i0}) = 1\times10^{13}$ cm^{-3}. Here, g_w is greater than the electron screening length $\lambda_{\rm De0}$ $(= 2.182\times10^{-5}$ cm) at $t = 0$ to ensure that two independent beams occur initially; the presence of two beams increases the possibility of observing well-controlled instabilities within the gap. The color intensity corresponds to the v_x. The time evolution shown in the four panels of Fig. 13 reveals that two well-defined beams are indeed formed and that they collide to form interpenetrating beams.

The phase dynamics associated with the real-space dynamics in Fig. 13 is shown in Fig. 14; the color intensity again corresponds to the v_x. Note that locally near $x = 0$ the phase-space structure takes the standard two-stream instability form: initially, the plasma exists as two cold beams because only the faster particles with a given sign of v_x meet in that region. As collisions occur between the counterpropagating beams, the phase space fills in. Recent MD work on such instabilities [79] suggests that instabilities will not occur in the gapped-slab SUNP studied here as a result of the strong electron screening, and further computational and experimental explorations are needed to tune the plasma parameters to create specific phenomena.

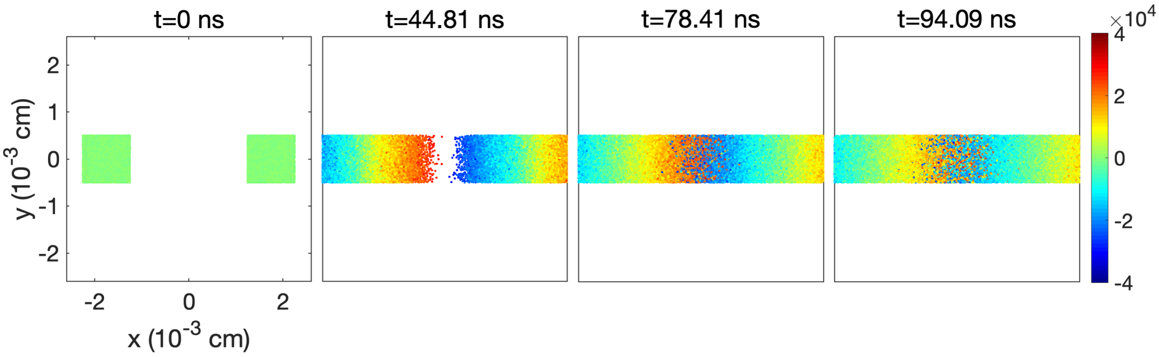

FIG. 13. Real-space evolution of a gapped-slab SUNP. The gapped-slab geometry, periodic in the y-z plane, is used to explore creating beams for studies of kinetic and hydrodynamic instabilities (e.g., two-stream, bump-on-tail, and Kelvin-Helmholtz), stopping power, and related phenomena. Particles are color coded by v_x. Note that the particles accelerate into the gap, and a beam collision occurs in the center. This geometry can be tuned by changing the spacing, density, and screening length to obtain further control.

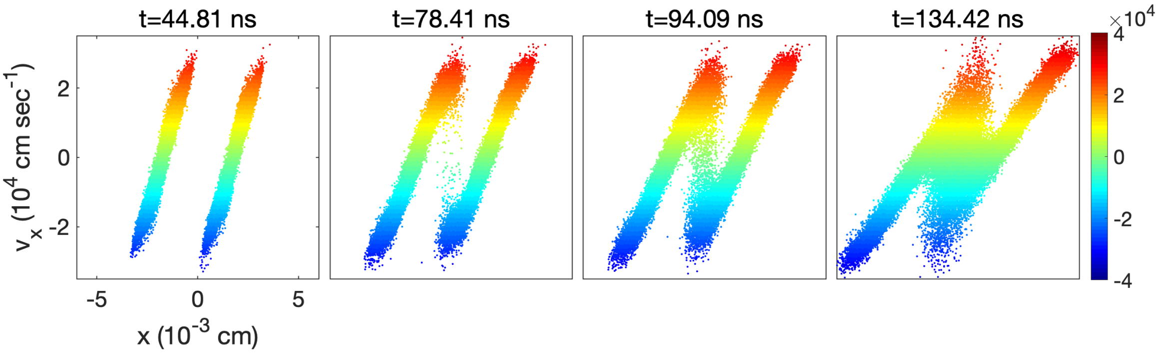

FIG. 14. Phase-space evolution of a gapped-slab SUNP. The equilibration of two colliding beams is shown in phase space, with time moving forward from the left panel to the right panel. Such a geometry can be used to study momentum-transfer processes, and potentially, if the collisionality were much lower, it could be used to study two-stream instabilities as well.

The energy balance of this plasma is shown in Fig. 15. While the potential energy within the ions is roughly constant, we see an initial increase in the ionic kinetic energy associated with the formation of the beams near the ends of the slabs. Note that, in contrast, the kinetic energy of the electrons decreases, which suggests that they increasingly screen the ions; however, all energy quantities become nearly constant after the beams meet.

VI. CONCLUSIONS AND OUTLOOK

We have explored the utility of SUNPs for examining a wide range of kinetic and hydrodynamic processes. We have developed a Yukawa-like model for SUNPs that accounts for plasma expansion and contraction, electron energetics, and a heterogeneous collisional background of electrons and neutrals. With this model, we examined three SUNP geometries: a solid rod, a hollow rod, and a gapped slab. Qualitatively, these three initial conditions have yielded structures in phase space that correspond to hydrodynamic expansion and implosion, nonlinear blastlike waves, and multiple beams, respectively.

We also explored our ability to control the "kineticness" of a plasma. By reducing the coupling parameter, a plasma can become kinetic, and in principle this can be controlled in a spatiotemporal fashion. We have used the *local* moment ratios (34) and (35) to quantify how kinetic a plasma is. Through computational studies such as those conducted in this paper, different levels of kineticness can be designed into plasma dynamics; for example, plasmas that span a range of kineticness spatially, specific kinetic phenomena (e.g., two-stream instability), and the quality of various hydrodynamic closures can be studied.

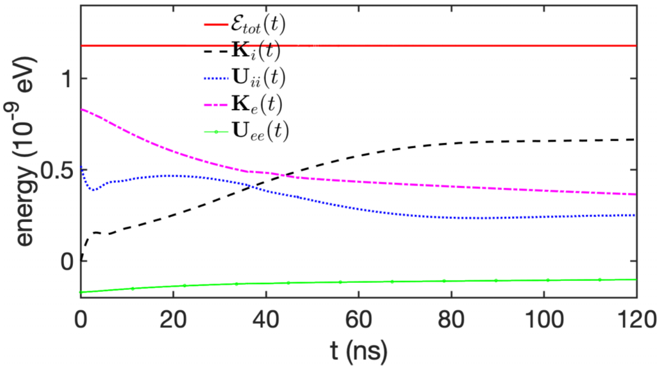

FIG. 15. Energy budget for the gapped-slab geometry. The budget is based on the terms in Eq. (17).

Our NEMD results have yielded several predictions. First, by choosing an initial geometry that allows for the faster tail particles to leave the main plasma in an evaporationlike process, leaving lower-velocity particles behind, we are able to increase the Coulomb coupling parameter to as large as 10. Also, consistent with the small values of transport coefficients in the strongly coupled regime [17], we find that SUNPs can be created to be nearly perfect fluids with moments consistent with drifting Maxwell-Boltzmann distributions and no heat flow. Conversely, as shown in the gapped-slab example, highly kinetic plasmas can also be formed. As shown in Fig. 10, new types of wave phenomena can be explored as well.

The results of this paper open several potential lines of inquiry, of which the most important is the further experimental exploration of SUNPs. Many other options remain to be explored computationally, including mixture SUNPs (which could be used to examine interdiffusive mixing processes), magnetic fields (which could potentially be used to study the physics of magnetized UNPs but also to exert additional confinement), tailoring laser-intensity profiles to ionize a gas at different times, using multiple lasers and masks to allow for noncylindrical initial densities, and so on. For example, a variable-density mask might be used to create a "plasma piston" that could produce a steady shock. Our SUNP model can also be improved to include more detailed electronic physics, including spatially varying screening and heat conduction; such a model could be built, for example, from a hybrid MD plus hydrodynamics model or an MD plus particle-in-cell model for the ion-electron system. In fact, for those regimes in which a SUNP is nearly a perfect fluid, a two-species hydrodynamics model would provide an accurate modeling tool. A combined experimental-computational model validation research effort is desirable.

ACKNOWLEDGMENTS

This work was supported by AFOSR Grant No. FA9550-17-1-0394. The authors thank Lisa Murillo for careful editing of the paper.

[1] S. Ichimaru, Strongly coupled plasmas: High-density classical plasmas and degenerate electron liquids, Rev. Mod. Phys. **54**, 1017 (1982).
[2] H. M. Van Horn, Dense astrophysical plasmas, Science **252**, 384 (1991).
[3] A. Diaw and M. S. Murillo, A dynamic density functional theory approach to diffusion in white dwarfs and neutron star envelopes, ApJ **829**, 16 (2016).
[4] J. F. Benage, W. R. Shanahan, and M. S. Murillo, Electrical Resistivity Measurements of Hot Dense Aluminum, Phys. Rev. Lett. **83**, 2953 (1999).
[5] B. A. Remington, R. P. Drake, and D. D. Ryutov, Experimental astrophysics with high power lasers and z pinches, Rev. Mod. Phys. **78**, 755 (2006).
[6] D. D. Ryutov, M. S. Derzon, and M. K. Matzen, The physics of fast *z* pinches, Rev. Mod. Phys. **72**, 167 (2000).
[7] R. Betti and O. A. Hurricane, Inertial-confinement fusion with lasers, Nat. Phys. **12**, 435 (2016).
[8] G. Gregori, S. B. Hansen, R. Clarke, R. Heathcote, M. H. Key, J. King, R. I. Klein, N. Izumi, A. J. Mackinnon, S. J. Moon *et al.*, Experimental characterization of a strongly coupled solid density plasma generated in a short-pulse laser target interaction, Contrib. Plasma Phys. **45**, 284 (2005).
[9] M. S. Murillo, Ultrafast Dynamics of Strongly Coupled Plasmas, Phys. Rev. Lett. **96**, 165001 (2006).
[10] E. G. Saiz, G. Gregori, D. O. Gericke, J. Vorberger, B. Barbrel, R. J. Clarke, R. R. Freeman, S. H. Glenzer, F. Y. Khattak, M. Koenig *et al.*, Probing warm dense lithium by inelastic x-ray scattering, Nat. Phys. **4**, 940 (2008).
[11] T. G. White, J. Vorberger, C. R. D. Brown, B. J. B. Crowley, P. Davis, S. H. Glenzer, J. W. O. Harris, D. C. Hochhaus, S. Le Pape, T. Ma *et al.*, Observation of inhibited electron-ion coupling in strongly heated graphite, Sci. Rep. **2**, 889 (2012).
[12] C. R. D. Brown, D. O. Gericke, M. Cammarata, B. I. Cho, T. Döppner, K. Engelhorn, E. Förster, C. Fortmann, D. Fritz, E. Galtier *et al.*, Evidence for a glassy state in strongly driven carbon, Sci. Rep. **4**, 5214 (2014).
[13] S. Tanaka and S. Ichimaru, Dynamic theory of correlations in strongly coupled, classical one-component plasmas: Glass transition in the generalized viscoelastic formalism, Phys. Rev. A **35**, 4743 (1987).
[14] Y. Rosenfeld, Equation of state and correlation functions of strongly coupled plasma mixtures: Density functional theory and analytic models, Phys. Rev. E **54**, 2827 (1996).
[15] J. Vorberger, I. Tamblyn, B. Militzer, and S. A. Bonev, Hydrogen-helium mixtures in the interiors of giant planets, Phys. Rev. B **75**, 024206 (2007).
[16] G. Chabrier and A. Y. Potekhin, Equation of state of fully ionized electron-ion plasmas, Phys. Rev. E **58**, 4941 (1998).
[17] L. G. Stanton and M. S. Murillo, Ionic transport in high-energy-density matter, Phys. Rev. E **93**, 043203 (2016).
[18] K. Y. Sanbonmatsu and M. S. Murillo, Shear Viscosity of Strongly Coupled Yukawa Systems on Finite Length Scales, Phys. Rev. Lett. **86**, 1215 (2001).
[19] S. Ichimaru, H. Iyetomi, and S. Tanaka, Statistical physics of dense plasmas: Thermodynamics, transport coefficients and dynamic correlations, Phys. Rep. **149**, 91 (1987).
[20] J. Lindl, Development of the indirect-drive approach to inertial confinement fusion and the target physics basis for ignition and gain, Phys. Plasmas **2**, 3933 (1995).
[21] X. L. Zhang, R. S. Fletcher, and S. L. Rolston, Observation of an Ultracold Plasma Instability, Phys. Rev. Lett. **101**, 195002 (2008).
[22] M. Marciante and M. S. Murillo, Thermodynamic and Kinetic Properties of Shocks in Two-Dimensional Yukawa Systems, Phys. Rev. Lett. **118**, 025001 (2017).
[23] T. C. Killian, Ultracold neutral plasmas, Science **316**, 705 (2007).
[24] T. C. Killian, S. Kulin, S. D. Bergeson, L. A. Orozco, C. Orzel, and S. L. Rolston, Creation of an Ultracold Neutral Plasma, Phys. Rev. Lett. **83**, 4776 (1999).
[25] S. Kulin, T. C. Killian, S. D. Bergeson, and S. L. Rolston, Plasma Oscillations and Expansion of an Ultracold Neutral Plasma, Phys. Rev. Lett. **85**, 318 (2000).
[26] M. P. Robinson, B. L. Tolra, M. W. Noel, T. F. Gallagher, and P. Pillet, Spontaneous Evolution of Rydberg Atoms Into an Ultracold Plasma, Phys. Rev. Lett. **85**, 4466 (2000).
[27] J. P. Morrison, C. J. Rennick, J. S. Keller, and E. R. Grant, Evolution from a Molecular Rydberg Gas to an Ultracold Plasma in a Seeded Supersonic Expansion of NO, Phys. Rev. Lett. **101**, 205005 (2008).
[28] M. Lyon, S. D. Bergeson, A. Diaw, and M. S. Murillo, Using higher ionization states to increase Coulomb coupling in an ultracold neutral plasma, Phys. Rev. E **91**, 033101 (2015).
[29] T. Sprenkle, A. Dodson, Q. McKnight, R. Spencer, S. Bergeson, A. Diaw and M. S. Murillo, Ion friction at small values of the Coulomb logarithm, Phys. Rev. E **99**, 053206 (2019).
[30] P. McQuillen, J. Castro, and T. C. Killian, High-resolution ionization of ultracold neutral plasmas, J. Phys. B **44**, 184013 (2011).
[31] P. McQuillen, J. Castro, and T. C. Killian, Collective modes in sculpted ultracold neutral plasmas, J. Phys. Conf. Ser. **388**, 122007 (2012).
[32] S. Laha, P. Gupta, C. E. Simien, H. Gao, J. Castro, T. Pohl, and T. C. Killian, Experimental Realization of an Exact Solution to the Vlasov Equations for an Expanding Plasma, Phys. Rev. Lett. **99**, 155001 (2007).
[33] M. S. Murillo, Using Fermi Statistics to Create Strongly Coupled Ion Plasmas in Atom Traps, Phys. Rev. Lett. **87**, 115003 (2001).
[34] Y. C. Chen, C. E. Simien, S. Laha, P. Gupta, Y. N. Martinez, P. G. Mickelson, S. B. Nagel, and T. C. Killian, Electron Screening and Kinetic-Energy Oscillations in a Strongly Coupled Plasma, Phys. Rev. Lett. **93**, 265003 (2004).
[35] T. Pohl, T. Pattard, and J. M. Rost, Kinetic modeling and molecular dynamics simulation of ultracold neutral plasmas including ionic correlations, Phys. Rev. A **70**, 033416 (2004).
[36] T. Pohl, T. Pattard, and J. M. Rost, Coulomb Crystallization in Expanding Laser-Cooled Neutral Plasmas, Phys. Rev. Lett. **92**, 155003 (2004).
[37] F. Robicheaux and J. D. Hanson, Simulation of the Expansion of an Ultracold Neutral Plasma, Phys. Rev. Lett. **88**, 055002 (2002).
[38] L. G. Stanton, J. N. Glosli, and M. S. Murillo, Multiscale Molecular Dynamics Model for Heterogeneous Charged Systems, Phys. Rev. X **8**, 021044 (2018).
[39] R. L. Liboff, Transport coefficients determined using the shielded Coulomb potential, Phys. Fluids **2**, 40 (1959).

[40] N. W. Ashcroft and D. Stroud, Theory of the thermodynamics of simple liquid metals, in *Solid State Physics*, Vol. 33 (Elsevier, Amsterdam, 1978), pp. 1–81.

[41] J. D. Huba, NRL plasma formulary 2009, NRL Technical Report, 2009 (unpublished).

[42] G. Parisi, *Statistical Field Theory* (Addison-Wesley, Reading, MA, 1988).

[43] J. L. Beauchamp, Theory of collision-broadened ion cyclotron resonance spectra, J. Chem. Phys. **46**, 1231 (1967).

[44] D. Wobschall, J. R. Graham, Jr., and D. P. Malone, Ion cyclotron resonance and the determination of collision cross sections, Phys. Rev. **131**, 1565 (1963).

[45] P. Langevin, A fundamental formula of kinetic theory, Ann. Chem. Phys. **5**, 245 (1905).

[46] T. Su and M. T. Bowers, Ion-polar molecular collisions: The average quadrupole orientation theory, Int. J. Mass Spectrom. Ion Phys. **17**, 309 (1975).

[47] M. He, D. Guo, Y. Feng, X. Xiong, H. Zhang, X. Fang, and W. Xu, Realistic modeling of ion-neutral collisions in quadrupole ion traps, J. Mass Spectrom. **50**, 95 (2015).

[48] D. H. E. Dubin and T. M. O'Neil, Trapped nonneutral plasmas, liquids, and crystals (the thermal equilibrium states), Rev. Mod. Phys. **71**, 87 (1999).

[49] K.-C. Ng, Hypernetted chain solutions for the classical one-component plasma up to $\gamma = 7000$, J. Chem. Phys. **61**, 2680 (1974).

[50] M. S. Murillo, Ultrafast dynamics of neutral, ultracold plasmas, Phys. Plasmas **14**, 055702 (2007).

[51] R. L. Liboff, *Kinetic Theory* (Wiley, New York, 1998).

[52] J. L. Nagle, I. G. Bearden, and W. A. Zajc, Quark-gluon plasma at the RHIC and the LHC: Perfect fluid too perfect? New J. Phys. **13**, 075004 (2011).

[53] G. Faussurier, S. B. Libby, and P. L. Silvestrelli, The viscosity to entropy ratio: From string theory motivated bounds to warm dense matter transport, High Energy Density Phys. **12**, 21 (2014).

[54] S. Plimpton, Fast parallel algorithms for short-range molecular dynamics, J. Comput. Phys. **117**, 1 (1995).

[55] R. R. Teachout and R. T. Pack, At. Data Nucl. Data Tables **3**, 195 (1971).

[56] M. Lyon, S. D. Bergeson, and M. S. Murillo, Limit of strong ion coupling due to electron shielding, Phys. Rev. E **87**, 033101 (2013).

[57] D. O. Gericke and M. S. Murillo, Disorder-induced heating of ultracold plasmas, Contrib. Plasma Phys. **43**, 298 (2003).

[58] See Supplemental Material at http://link.aps.org/supplemental/10.1103/PhysRevE.101.023207 for a visualization of the plasma dynamics, coarse graining, and time-evolving plasma parameters for this scenario.

[59] T. K. Langin, G. M. Gorman, and T. C. Killian, Laser cooling of ions in a neutral plasma, Science **363**, 61 (2019).

[60] N. Komatsu and T. Abe, Expansion shock waves in the implosion process from a time-reversible molecular-dynamics simulation of a dual explosion process, Phys. Fluids **19**, 056103 (2007).

[61] P. Gaspard and J. Lutsko, Imploding shock wave in a fluid of hard-core particles, Phys. Rev. E **70**, 026306 (2004).

[62] W. G. Hoover, Structure of a Shock-Wave Front in a Liquid, Phys. Rev. Lett. **42**, 1531 (1979).

[63] B. L. Holian, W. G. Hoover, B. Moran, and G. K. Straub, Shock-wave structure via nonequilibrium molecular dynamics and Navier-Stokes continuum mechanics, Phys. Rev. A **22**, 2798 (1980).

[64] E. Salomons and M. Mareschal, Usefulness of the Burnett Description of Strong Shock Waves, Phys. Rev. Lett. **69**, 269 (1992).

[65] T. E. Itina, J. Hermann, P. Delaporte, and M. Sentis, Laser-generated plasma plume expansion: Combined continuous-microscopic modeling, Phys. Rev. E **66**, 066406 (2002).

[66] F. Garrelie, J. Aubreton, and A. Catherinot, Monte Carlo simulation of the laser-induced plasma plume expansion under vacuum: Comparison with experiments, J. Appl. Phys. **83**, 5075 (1998).

[67] T. Schätz, U. Schramm, and D. Habs, Crystalline ion beams, Nature (London) **412**, 717 (2001).

[68] J. P. Schiffer, Crystalline beams, in *Proceedings of the Particle Accelerator Conference* (IEEE, New York, 1995), Vol. 5, pp. 3164–3166.

[69] P. G. Drazin, *Introduction to Hydrodynamic Stability*, Cambridge Texts in Applied Mathematics, Vol. 32 (Cambridge University, Cambridge, England, 2002).

[70] S. Chandrasekhar, *Hydrodynamic and Hydromagnetic Stability* (Courier, New York, 2013).

[71] D. H. Sharp, Overview of Rayleigh-Taylor instability, LANL Technical Report, 1983 (unpublished).

[72] P. A. Sturrock, *Plasma Physics: An Introduction to the Theory of Astrophysical, Geophysical and Laboratory Plasmas* (Cambridge University, Cambridge, England, 1994).

[73] S. P. Sarraf, E. A. Williams, and L. M. Goldman, Ion-ion two-stream instability in multispecies laser-produced plasma, Phys. Rev. A **27**, 2110 (1983).

[74] N. Kim, J. Song, H. Roh, Y. Jang, S. Ryu, S. Huh, and G. Kim, Ion-neutral collision effect on ion-ion two-stream-instability near sheath-presheath boundary in two-ion-species plasmas, Plasma Sources Sci. Technol. **26**, 06LT01 (2017).

[75] P. H. Diamond, S.-I. Itoh, and K. Itoh, *Modern Plasma Physics: Volume 1, Physical Kinetics of Turbulent Plasmas* (Cambridge University, Cambridge, England, 2010).

[76] O. Boine-Frankenheim and J. D'Avanzo, Stopping power of ions in a strongly magnetized plasma, Phys. Plasmas **3**, 792 (1996).

[77] C. F. Clauser and N. R. Arista, Stopping power of dense plasmas: The collisional method and limitations of the dielectric formalism, Phys. Rev. E **97**, 023202 (2018).

[78] S. Skupsky, Energy loss of ions moving through high-density matter, Phys. Rev. A **16**, 727 (1977).

[79] J. J. Williams, G. Dharuman, M. Marciante, J. H. Cooley, and M. S. Murillo, Bump-on-tail instability across coupling and interaction-range regimes, Phys. Rev. Res. **1**, 033166 (2019).